Applied Catalysis B: Environmental 200 (2017) 521–529

Contents lists available at ScienceDirect

Applied Catalysis B: Environmental

journal homepage: www.elsevier.com/locate/apcatb

Cu doped OL-1 nanoflower: A UV–vis-infrared light-driven catalyst for gas-phase environmental purification with very high efficiency

Min Zeng, Yuanzhi Li*, Fang Liu, Yi Yang, Mingyang Mao, Xiujian Zhao

State Key Laboratory of Silicate Materials for Architectures, Wuhan University of Technology, 122 Luoshi Road, Wuhan 430070, PR China

ARTICLE INFO

Article history:
Received 16 June 2016
Received in revised form 19 July 2016
Accepted 23 July 2016
Available online 28 July 2016

Keywords:
Cu doped OL-1 nanoflower
Full solar spectrum catalysis
Infrared catalysis
Photoactivation
Catalytic oxidation

ABSTRACT

The nanoflowers of Cu doped octahedral layered birnessite (Cu-OL-1) were prepared by a facile method of hydrothermal redox reaction between $Cu(NO_3)_2$, $Mn(NO_3)_2$, and $KMnO_4$. The Cu-OL-1 samples were characterized by XRD, TEM, SEM, ICP, BET, etc. Remarkably, the Cu-OL-1 exhibits very high catalytic activity for the abatement of air pollutants (e.g. CO and benzene) with the irradiation of full solar spectrum, visible-infrared, or infrared light. The high catalytic activity of Cu-OL-1 originates from the efficient solar light-driven thermocatalysis, which is attributed to its high thermocatalytic activity and strong absorption in the whole solar spectrum region. The Cu doping in OL-1 significantly enhances its thermocatalytic activity due to a considerable enhancement in the activity of lattice oxygen in OL-1. A conceptually novel photoactivation different from the conventional photoactivation on semiconductors (e.g. TiO_2) is found to enhance the activity of lattice oxygen in OL-1, thus accelerating the thermocatalysis on Cu-OL-1. We reveal the origin of the novel photoactivation by CO temperature-programmed reduction in dark and with solar light irradiation, and density functional theory (DFT) calculations.

1. Introduction

Solar energy is an inexhaustible and renewable energy on the Earth. The efficient utilization of the solar energy for solar cells, photocatalytic environmental purification, photocatalytic synthesis of chemicals and fuels (e.g. H_2), etc., has been attracting intensive interest for decades. Reported works in this area have mainly focused on the utilization of UV and visible light based on semiconducting materials [1–18]. In contrast to the works on the utilization of UV–vis light, studies aimed at utilizing infrared light that constitutes about 50% of the incoming solar energy are quite limited [19–37]. Generally, the reported strategies of utilizing infrared light for photocatalysis are based on the conventional photocatalysis principle of semiconductors [1,38]: The absorption of photons with energy higher than the band gap (E_g) of the semiconductor excites the electrons in the valence band to the conduction band, leaving holes in the valence band. The photogenerated electrons and holes induce redox reaction of the reactants. The most used strategy is to form composites of semiconducting photocatalysts with upconversion materials such as rare earth metal ions, carbon quantum dots, etc., which converse infrared light to UV or visible light to activate the semiconducting photocatalysts [22–32]. Infrared laser with high light intensity is usually required to activate the upconversion photocatalysts [24–28]. Due to the narrow absorption band in near-infrared region as well as low upconversion efficiency at moderate light intensity for the upconversion materials [33], it is challenging to realize infrared photocatalytic purification with high efficiency on the upconversion photocatalysts.

Another strategy is to prepare infrared responsive photocatalysts by reducing E_g of semiconducting photocatalysts to infrared energy region, such as PbSe/CdSe/CdS [34], $Cu_2(OH)PO_4$ [35], WS_2 nanosheet [36], Bi_2WO_6/TiO_2 [37], etc. The challenge for the strategy is how to increase the total solar energy utilization efficiency as all UV and visible photon energy in excess of E_g is lost via electron-phonon interactions [39], and achieve a compromise between wide infrared absorption and adequate redox capability of the photogenerated electrons and holes [40].

Herein, we developed a facile approach of hydrothermal redox reaction to prepare Cu doped OL-1 nanoflowers with different Cu doping amount. Remarkably, the Cu doped OL-1 nanoflowers exhibit catalytic activity with very high efficiency for the oxidation of poisonous CO and benzene (typical organic air pollutants) under the irradiation of full solar spectrum, visible-infrared, or infrared light. The high catalytic activity of the Cu doped OL-1 nanoflowers is ascribed to its high thermocatalytic activity and strong absorption in the whole solar spectrum region, resulting in the efficient solar

* Corresponding author.
E-mail addresses: liyuanzhi66@hotmail.com, liyuanzhi@whut.edu.cn (Y. Li).

http://dx.doi.org/10.1016/j.apcatb.2016.07.042
0926-3373/

light-driven thermocatalysis. The Cu doping in OL-1 significantly improves the thermocatalytic activity of OL-1. A novel photoactivation, which is different from the conventional photoactivation or photocatalysis on semiconducting photocatalysts (e.g. TiO_2), is found to accelerate the solar light-driven thermocatalysis on the Cu doped OL-1 nanoflowers. We reveal the origin of the thermocatalytic enhancement induced by the Cu doping in OL-1 and the novel photoactivation by combining both experimental and theoretical evidence.

2. Experimental section

2.1. Preparation

The Cu^{2+} ion doped OL-1 samples with different amount of Cu were prepared by a facile method of hydrothermal redox reaction between $Cu(NO_3)_2{\cdot}3H_2O$, $Mn(NO_3)_2$, and $KMnO_4$. The detailed procedure was as follows: a known amount of $Cu(NO_3)_2{\cdot}3H_2O$ (e.g. 0, 0.4168, 0.8335, 1.6670, 2.0838 g) and 7.1580 g of $Mn(NO_3)_2$ (50 wt%) was dissolved in 80 mL of distilled water in a beaker under magnetic stirring. 6.3212 g of $KMnO_4$ was added into the $Mn(NO_3)_2$ and $Cu(NO_3)_2$ aqueous solution under magnetic stirring until it was dissolved. The beaker was covered with polyethylene film and placed in an electrical oven. The solution in the beaker was heated to 50 °C and kept at the temperature for 60 h. After the beaker cooled to ambient temperature, the precipitate was filtered, thoroughly washed with distilled water, and dried at 50 °C for 24 h.

2.2. Characterization

X-ray diffraction (XRD) patterns of the samples were recorded obtained on a RigakuDmax X-ray diffractometer with Cu Kα radiation. Scanning electron microscopy (SEM) images were obtained on a ULTRA PLUS-43-13 scanning electron microscope. Transmission electron microscopy (TEM) images were acquired on a JEM-100CX electron microscope. The specific surface area of the samples was measured on ASAP2020 using N_2 adsorption at −196 °C. The chemical composition of the samples was measured by inductively coupled plasma/optical emission spectroscopy (ICP-OES, PerkinElmer, Optima 4300DV). The element valence state of the samples was analyzed on a VG Multilab 2000 X-ray photoelectron spectrometer (XPS) using Mg Kα radiation. Diffusive reflectance UV–vis (DRUV–vis) absorption spectra were recorded on a UV-3600 spectrophotometer using $BaSO_4$ powder as background reference.

CO temperature-programmed reduction (CO-TPR) of the sample in the dark or with the solar light irradiation was performed on a TP-5080 multifunctional adsorption apparatus equipped with a TCD detector. A quartz window was connected to one of the end of a quartz tube reactor. The details are described in our previous work [41].

2.3. Photothermocatalytic activity

The photothermocatalytic activity of the samples for CO oxidation was measured under steady state on a flow fixed cylindrical stainless steel reactor (447 mL) with a quartz window (110 mm in diameter) under the irradiation of the full solar spectrum, visible-infrared, or infrared irradiation from a Xe lamp, which has the spectral profile similar to the solar spectra [42]. The details are described in our previous work [41]. A feed stream with 1.2 vol% CO, which was generated by mixing a flow of 5 vol% CO/He and a flow of 20.8 vol% O_2/N_2, flowed into the reactor at a flow rate of 40 mL min^{-1}. The light intensity of the full solar spectrum, visible-infrared, or infrared irradiation above 420, 480, 560, 690, or 830 nm is 179.4, 166.9, 150.8, 138.7, 125.6, 122.4 mW cm^{-2}, respectively.

The procedure of measuring the photothermocatalytic activity of the samples for benzene oxidation under the irradiation of the Xe lamp was described in our previous works [42,43]. The amount of the sample was 0.1000 g and the amount of benzene injected in to the reactor was 8.0 μL. In this case, the light intensity of the full solar spectrum, visible-infrared and infrared irradiation above 420, 480, 560, 690, or 830 nm is 311.7, 303.9, 278.2, 263.4, 246.3, 244.2 mW cm^{-2}, respectively.

The products and reactants were analyzed on a GC9560 gas chromatograph. The analysis condition by the gas chromatograph was detailed in our reported work [44,45].

2.4. Photocatalytic activity at near ambient temperature

The procedure of measuring the photocatalytic activity of the Cu-OL-C sample for CO oxidation under the irradiation of the Xe lamp is the same as that of the photothermocatalytic activity described above besides the following procedure: the Cu-OL-C sample was coated on a glass slide that was put on the bottom of the reactor. The reactor was placed in an ice-water bath to keep the reaction temperature at near ambient temperature under the irradiation of the Xe lamp.

2.5. Thermocatalytic activity and photothermocatalytic activity at the different temperature

The catalytic activity of the samples for CO oxidation at the different temperature in the dark or with the solar light irradiation was measured under steady state in a flow fixed quartz tube reactor on a WFS-2015 online gas-phase reaction apparatus. A quartz window was connected to one of the end of the quartz tube reactor. The Xe lamp was placed in the front of the quartz window. A feed stream with 1.0 vol% CO, which was generated by mixing a flow of 5 vol% CO/He and a flow of 20.8 vol% O_2/N_2, flowed into the reactor. The details are described in our previous work [41].

2.6. DFT calculation method

Density functional theory (DFT) calculations were performed to study the Cu doped OL-1 by using the Perdew–Burke–Ernzerhof functional and Projected Augmented Wave (PAW) pseudopotentials [46,47] as embedded in the Vienna Ab-initio Simulation Package (VASP 5.3). In order to properly describe the localization of 3d electrons of Mn and Cu, orbital-dependent corrections using the DFT + U method were introduced to account for the strong on-site Coulomb repulsion among the localized 3d electrons. We used the Mn3d U^{eff} value of 3.9 eV and Cu3d U^{eff} value of 3.0 eV (PBE + U), which were in accordance to the corresponding value reported [48,35]. In relaxation, summations over the Brillouin zone (BZ) were performed with a 2 × 2 × 2 Monkhorst-Pack k-point mesh. The smooth part of the wave functions was expanded in plane waves with a kinetic energy cutoff of 400 eV, and the convergence criteria for the electronic and ionic relaxation were 10^{-4} eV and 10^{-3} eV $Å^{-1}$, respectively.

3. Results and discussion

3.1. Preparation and characterization

The Cu doped OL-1 samples with the Cu/Mn atomic ratio of 0, 0.029, 0.058, 0.115, 0.144 in the reactants were prepared by a facile method of hydrothermal redox reaction between $Cu(NO_3)_2$, $KMnO_4$ and $Mn(NO_3)_2$ at 50 °C. The obtained Cu doped OL-1 samples are denoted as OL-1, Cu-OL-A, Cu-OL-B, Cu-OL-C, Cu-OL-D, respectively. The samples were characterized by XRD, SEM, TEM, BET, ICP, XPS, etc. The XRD analysis reveals that all the pure OL-1

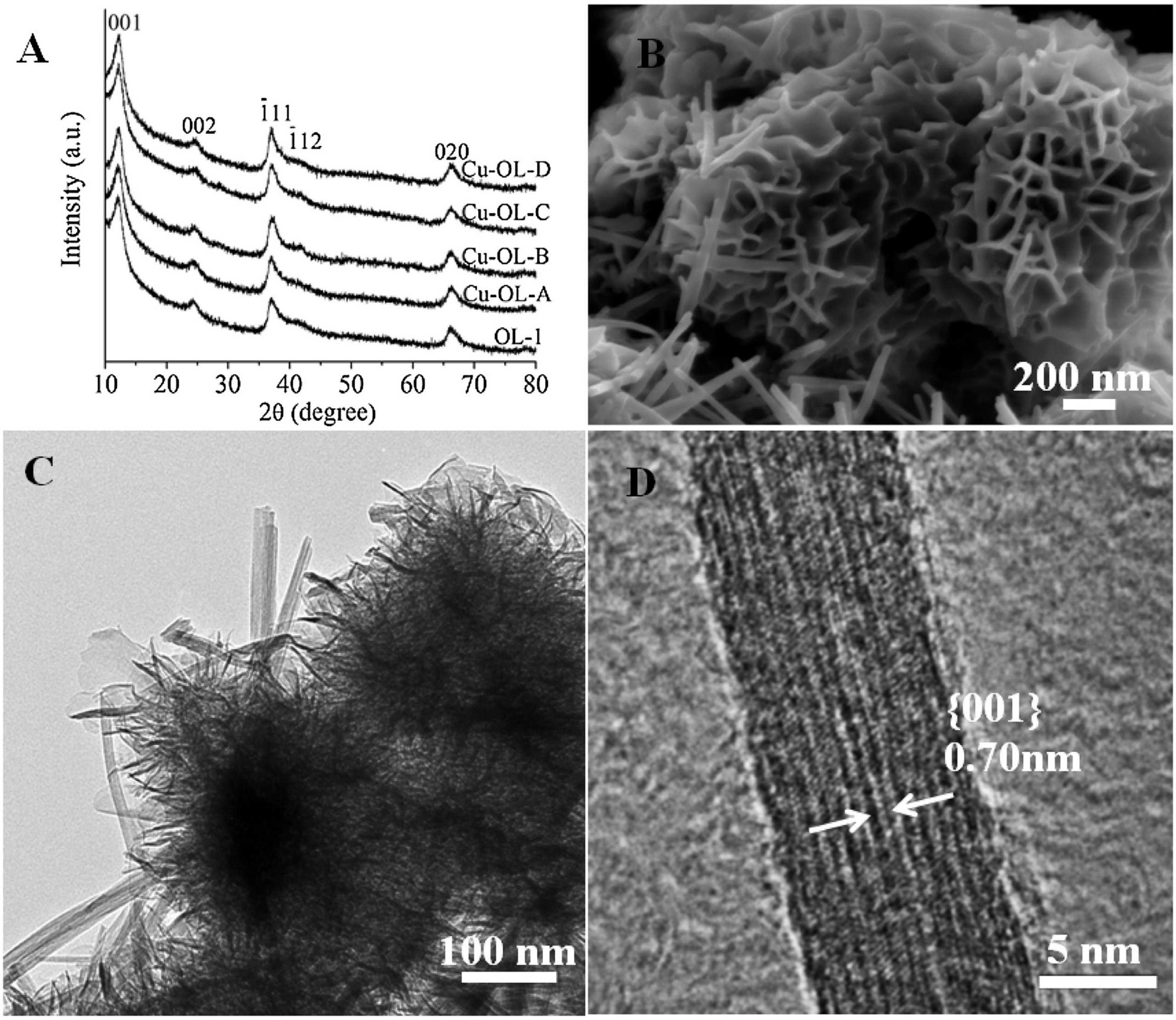

Fig. 1. XRD patterns of the Cu doped OL-1 samples (A). SEM (B) and TEM (C, D) images of Cu-OL-C.

and Cu doped OL-1 samples exhibit a pure octahedral layered birnessite structure ($K_{0.46}Mn_2O_4$(OL-1), JCPDS 80-1098), which is a type of manganese oxide that has edge-shared MnO_6 octahedral forming a two-dimensional (2D) layer structure with exchangeable cations (e.g. K^+) located at the interlayer space [41,49]. No crystalline phase of CuO is observed (Fig. 1A). This result indicates that the Cu doping does not give rise to any change in the birnessite structure of OL-1. The average crystal size for the samples is calculated according to the Scherrer formula ($L = 0.89\,\lambda/\beta\,\cos\theta$) at $2\theta = 12.3^\circ$ (corresponding to {001} facet). The average crystal size of OL-1, Cu-OL-A, Cu-OL-B, Cu-OL-C, and Cu-OL-D is 6.4, 6.4, 6.4, 6.5, 6.4 nm, respectively.

The morphology of the Cu doped OL-1 samples was characterized by SEM and TEM. The Cu doped OL-1 sample (Cu-OL-C) is characterized by a nanoflower-like morphology consisted of interwoven nanoflakes, among which there are many microsized pores (Fig. 1B). The thickness of nanoflakes is 4.5–18.2 nm, which is in general agreement to the average crystal size corresponding to {001} facets obtained by XRD. TEM images confirm the morphology of Cu-OL-C observed by SEM (Fig. 1C). HRTEM image on the side of a nanoflake exhibits {001} facet with lattice spacing of 0.70 nm (Fig. 1D). All the pure OL-1 and other Cu doped OL-1 samples have similar nanoflower-like morphology consisted of interwoven nanoflakes (Supplementary information, Figs. S1–S3). The BET surface area of pure OL-1, Cu-OL-A, Cu-OL-B, Cu-OL-C, and Cu-OL-D, measured by N_2 adsorption (Fig. S4), is 227.5, 202.9, 241.1, 224.9, 241.7 $m^2\,g^{-1}$, respectively (Table 1).

The chemical composition of the samples was determined by the inductively coupled plasma-optical emission spectroscopy (ICP-OES). As shown in Table 1, the K/Mn atomic ratio of the pure OL-1 sample is 0.092. The Cu doping in OL-1 leads to a decrease in the K/Mn atomic ratio for the Cu doped OL-1 samples. When the initial Cu/Mn atomic ratio in the reactants is 0.029 and 0.058, the K/Mn atomic ratio in the obtained Cu-OL-A and Cu-OL-B decreases from 0.092 to 0.076, 0.066, respectively. The Cu/Mn atomic ratio of Cu-OL-A and Cu-OL-B is 0.028, 0.052, respectively, which is very close to the corresponding Cu/Mn atomic ratio in the reactants. This result reveals that Cu dopes into OL-1. When the Cu/Mn atomic ratio in the reactants further increases to 0.115 and 0.144, the K/Mn atomic ratio of Cu-OL-C and Cu-OL-D slightly decreases to 0.054, 0.051, while their Cu/Mn atomic ratio slightly increases to 0.080, 0.089, respectively. The similar composition of Cu-OL-C and Cu-OL-D indicates that Cu in OL-1 reaches to its maximum doping amount.

Table 1
The BET surface area, atomic ratio, and thermoscatalytic activity of the samples.

Sample	Surface area ($m^2\ g^{-1}$)	Atomic ratio				Thermocatalytic activity		
		Cu/Mn in reactants	Cu/Mn by ICP	K/Mn by ICP	Mn^{3+}/Mn^{4+} by XPS	$T_{light\text{-}off}$	T_{50}	T_{90}
OL-1	227.5	0	0.000	0.092	2.03	∼100	157	194
Cu-OL-A	202.9	0.029	0.028	0.076	2.24	∼40	130	159
Cu-OL-B	241.1	0.058	0.052	0.066	2.45	∼40	112	142
Cu-OL-C	224.9	0.115	0.080	0.054	2.59	∼40	103	135
Cu-OL-D	241.7	0.144	0.089	0.051	2.59	∼40	106	136

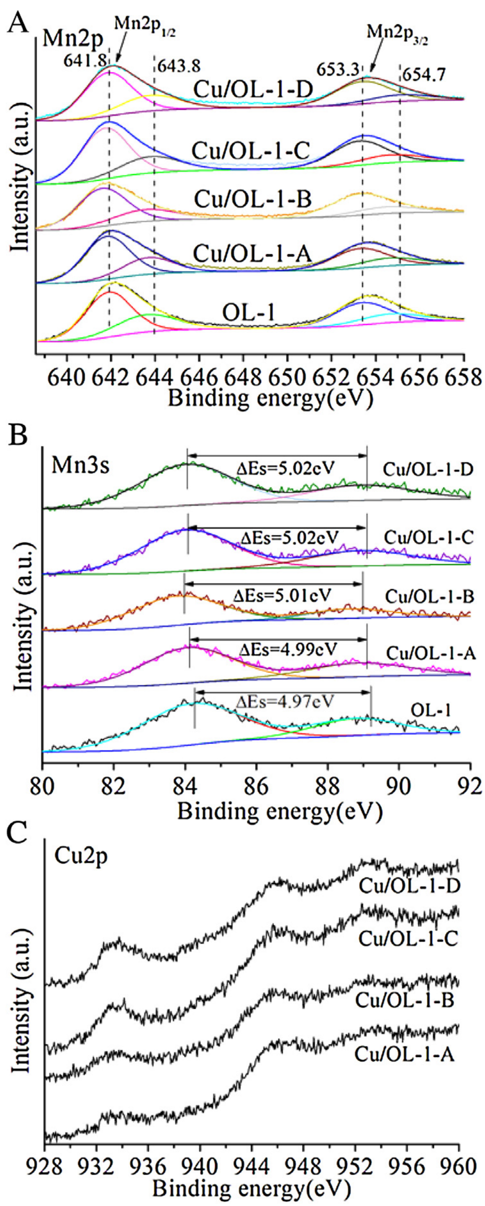

Fig. 2. Mn2p (A), Mn3s (B), and Cu2p (C) XPS spectra of the Cu ion doped OL-1 samples.

The oxidation state of Mn and Cu for the samples is qualitatively analyzed by studying the Mn2p, Mn3s, and Cu2p XPS spectra, respectively. The Mn2p spectra of all the pure OL-1 and Cu

ion doped OL-1 samples are decomposed into four peaks (Fig. 2A). The peaks located at ∼641.8 and ∼653.3 eV are attributed to $Mn2p_{3/2}$ and $Mn2p_{1/2}$ of Mn^{3+} species, respectively. The peaks located at ∼643.8 and ∼654.7 eV are attributed to $Mn2p_{3/2}$ and $Mn2p_{1/2}$ of Mn^{4+} species [50]. No Mn^{2+} species are detected by XPS for all the pure OL-1 and Cu ion doped OL-1 samples. The atomic ratio of Mn^{3+}/Mn^{4+} was calculated by fitting the Mn2p spectra (Table 1). The Mn^{3+}/Mn^{4+} atomic ratio for the pure OL-1, Cu-OL-A, Cu-OL-B, Cu-OL-C, and Cu-OL-D is 2.03, 2.24, 2.45, 2.59, 2.59, respectively. The increase in the Mn^{3+}/Mn^{4+} atomic ratio with increasing the Cu/Mn atomic ratio is ascribed to the lower valence state of the doped Cu^{2+} ions than the Mn ions (Mn^{3+}, Mn^{4+}) in OL-1 to keep electrostatic balance in OL-1.

The average oxidation state (AOS) of Mn in the pure OL-1 and Cu doped OL-1 samples can be also determined by using the magnitude of Mn3 s multiplet splitting (ΔE_s) [50]:

$$\mathrm{AOS} = 8.95 - 1.13\Delta E_s(\mathrm{eV})$$

The ΔE_s of OL-1, Cu-OL-A, Cu-OL-B, Cu-OL-C, and Cu-OL-D is 4.97, 4.99, 5.01, 5.02 and 5.02 eV, respectively (Fig. 2B). Their corresponding AOS is calculated to be 3.33, 3.31, 3.29, 3.28, and 3.28, respectively.

The Cu2p spectra of the Cu ion doped OL-1 samples are shown in Fig. 2C. All the Cu doped OL-1 samples have two peaks around ∼933.3 and ∼953.5 eV, which are assigned to $Cu2p_{3/2}$ and $Cu2p_{1/2}$ of Cu^{2+} species [51], respectively. In addition, the Cu ion doped OL-1 samples have broad satellite peak around 942.0–948.6 eV, which is in general agreement to that of the Cu2p spectra for CuO [51]. The result indicates that Cu exists in the form of Cu^{2+} in all the Cu doped OL-1 samples.

3.2. Photothermocatalytic activity

3.2.1. CO purification

As the efficient optical absorption is prerequisite for photocatalysis, we measured the optical absorption of the samples. All the samples of the pure OL-1 and Cu doped OL-1 have strong absorption in the entire region of full solar spectrum from 240 to 2400 nm (Fig. 3A). The Cu doping does not give rise to an obvious evolution of the absorption spectra of OL-1. To clarify whether the strong absorption results in efficient photocatalysis, we measured the catalytic activity of the samples for the oxidation of CO (poisonous air pollutant) as a model reaction under the full solar spectrum irradiation from a Xe lamp. The samples of the pure OL-1 and Cu doped OL-1 exhibit efficient catalytic activity. The CO_2 production rate in the initial five minutes (r_{CO2}) of the pure OL-1 sample is 58.5 μmol g^{-1} min^{-1} (Fig. 3B). The Cu doping considerably increases the catalytic activity of OL-1. With increasing the Cu/Mn atomic ratio in the Cu doped OL-1 sample to 0.028 (Cu-OL-A), 0.052 (Cu-OL-B), 0.080 (Cu-OL-C), the r_{CO2} increases to 103.1, 125.4, 143.3 μmol g^{-1} min^{-1}, respectively. Further increasing the Cu/Mn atomic ratio to 0.089 leads to a slight decrease in the r_{CO2} of Cu-OL-D to 134.3 μmol g^{-1} min^{-1}. Compared to the pure OL-1, the r_{CO2} of Cu-OL-C with the highest catalytic activity increases by 2.4 times.

TiO_2 (P25) is a well-known benchmark photocatalyst. In order to make comparison, we measured the catalytic activity of TiO_2 (P25) for CO oxidation under conditions identical to the Cu doped OL-1 samples with the full solar spectrum irradiation. The r_{CO2} of TiO_2

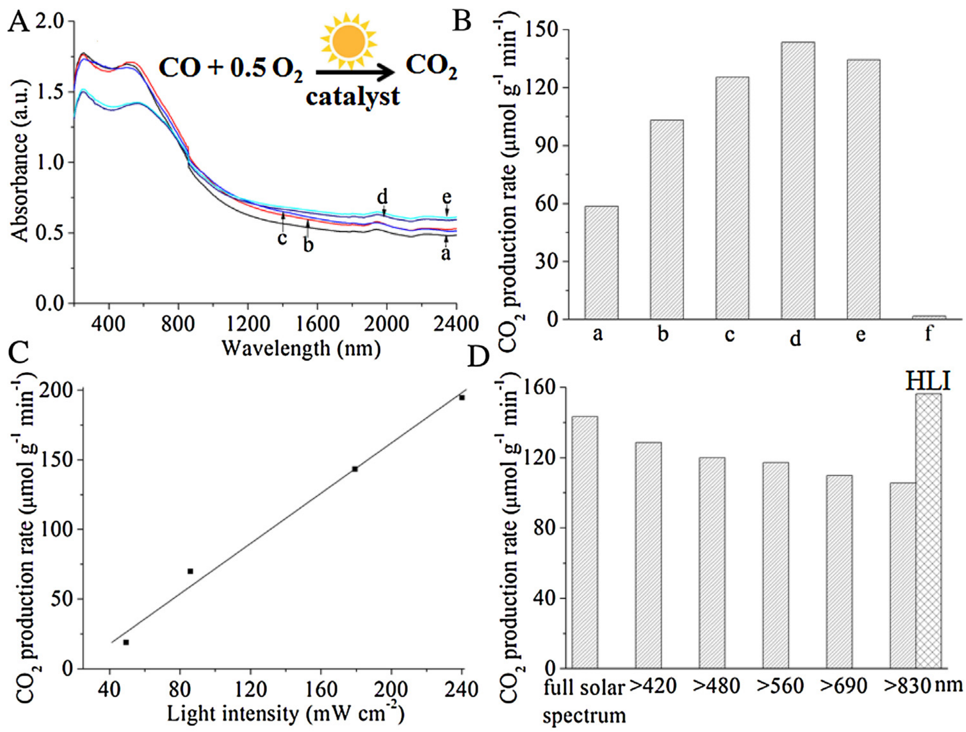

Fig. 3. The optical absorption spectra of the Cu doped OL-1 samples (A). The CO_2 production rate (r_{CO2}) of the samples for CO oxidation under the full solar spectrum irradiation with light intensity of 179.4 mW cm^{-2} (B). The r_{CO2} of Cu-OL-C under the full solar spectrum irradiation with different light intensity (C). The r_{CO2} of Cu-OL-C under the visible-infrared and infrared irradiation using different cut-off filters (D): OL-1(a), Cu-OL-A (b), Cu-OL-B (c), Cu-OL-C (d), Cu-OL-D (e), and TiO_2(P25) (f); HLI in Fig. 3D means higher light intensity (188.3 mW cm^{-2}).

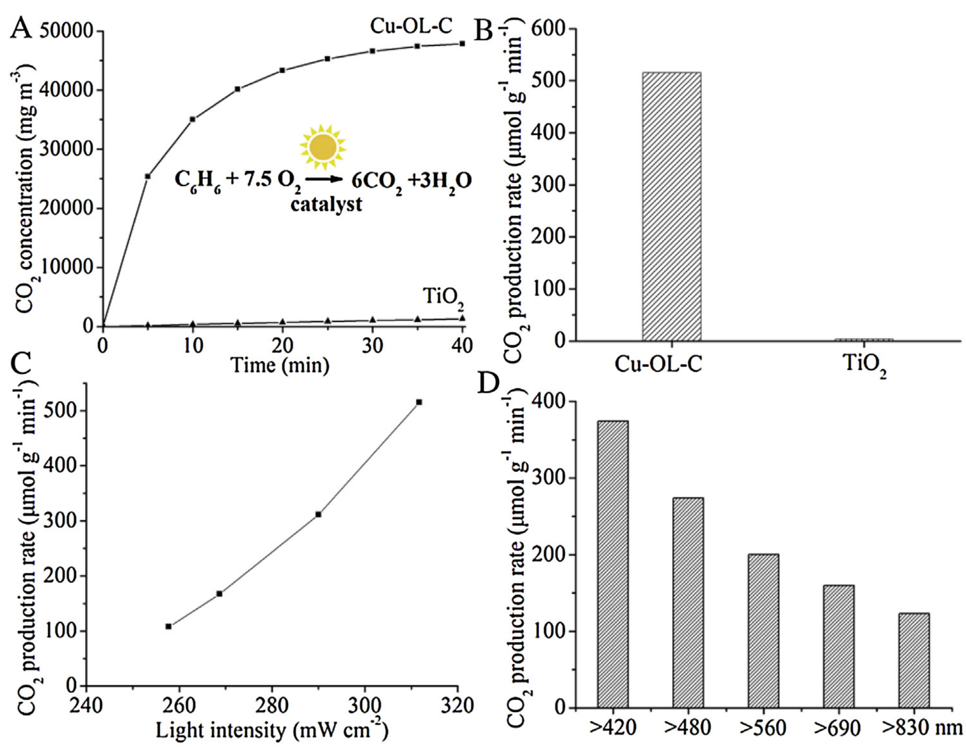

Fig. 4. CO_2 concentration evolution with the irradiation time over the samples for benzene oxidation under the full solar spectrum irradiation (A). The initial CO_2 production rate (r_{ICO2}, in initial five minutes) of the samples for benzene oxidation under the full solar spectrum irradiation with light intensity of 311.7 mW cm^{-2} (B). The r_{ICO2} of Cu-OL-C for benzene oxidation under the full solar spectrum irradiation with different light intensity (C). The r_{ICO2} of Cu-OL-C for benzene oxidation under the visible-infrared and infrared irradiation using different cut-off filters (D).

(P25) is 1.66 μmol g^{-1} min^{-1} (Fig. 3B), which is 86.4 times lower than that of Cu-OL-C.

We measured the catalytic activity of Cu-OL-C for CO oxidation under the full solar spectrum irradiation with different light

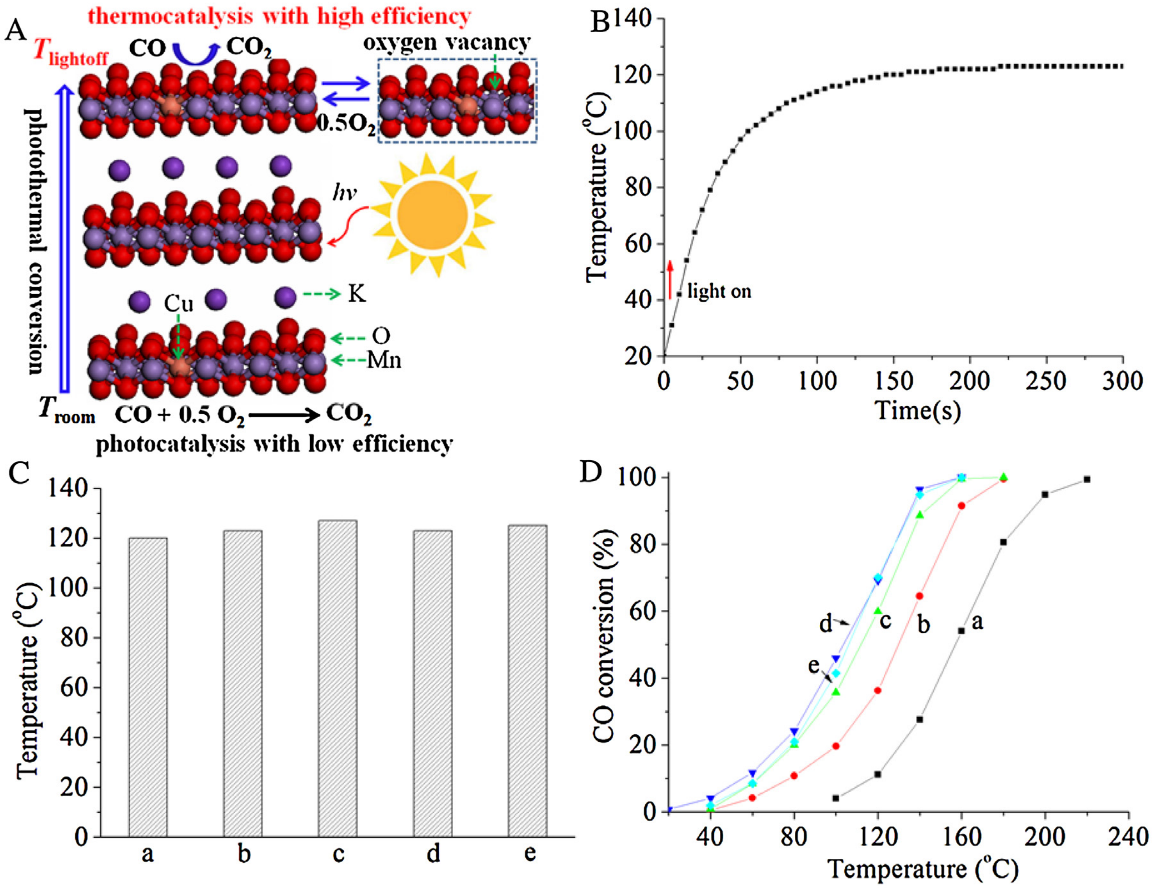

Fig. 5. Schematic illustration of the solar light-driven thermocatalysis on Cu doped OL-1 (A). The temperature evolution of Cu-OL-C (B) and equilibrium temperature of the Cu doped OL-1 samples (C) upon the full solar spectrum irradiation. Thermocatalytic activity of the Cu doped OL-1 samples at different temperature for CO oxidation under the condition of 1.0 vol% CO and 48000 mL $g^{-1}{}_{-catal}$ h^{-1} (D).

intensity (Fig. 3C). At the low light intensity of 49.4 mW cm^{-2}, Cu-OL-C still shows efficient catalytic activity with the r_{CO2} of 18.9 μmol g^{-1} min^{-1}. Increasing light intensity significantly enhances the catalytic activity of Cu-OL-C. When the light intensity increases to 85.9, 179.4, 240.2 mW cm^{-2}, the r_{CO2} of Cu-OL-C significantly increases to 70.0, 143.3, 194.6 μmol g^{-1} min^{-1}, respectively.

We measured the catalytic activity of Cu-OL-C for CO oxidation under the irradiation of visible-infrared or infrared light (Fig. 3D). Cu-OL-C exhibits efficient catalytic activity under the visible-infrared irradiation. Its r_{CO2} under the visible-infrared irradiation above 420, 480, 560, and 690 nm is 128.5, 119.9, 117.1, 109.7 μmol g^{-1} min^{-1}, respectively. Remarkably, even under the infrared irradiation above 830 nm, Cu-OL-C still shows very high catalytic activity with its r_{CO2} as high as 105.5 μmol g^{-1} min^{-1}. Compared to the higher catalytic activity under the full solar spectrum irradiation, the reduction in the catalytic activity under visible-infrared or infrared irradiation is ascribed to the reduction in the light intensity. To confirm it, we measured the catalytic activity of Cu-OL-C for CO oxidation under the infrared irradiation above 830 nm with higher light intensity. When the light intensity of the infrared irradiation increases from 122.4 to 188.3 mW cm^{-2}, its r_{CO2} increases from 105.5 to 156.2 μmol g^{-1} min^{-1}.

3.2.2. Benzene abatement

We also tested the catalytic activity of Cu-OL-C for the oxidation of the carcinogenic and recalcitrant benzene (a typical volatile organic air pollutant) with high oxidation potential (2.75 V vs. saturated Hg/Hg_2Cl_2 SCE) [52] under the solar light irradiation.

Under the full solar spectrum irradiation from the Xe lamp, benzene is quickly oxidized to CO_2 on the Cu-OL-C sample (Fig. 4A). Its initial CO_2 production rate (r_{ICO2}, in the initial five minutes) is as high as 515.3 μmol g^{-1} min^{-1} (Fig. 4B). In striking contrast, under the full solar spectrum irradiation, the photocatalytic oxidation of benzene on TiO_2 (P25) is very slow (Fig. 4A). The r_{ICO2} of Cu-OL-C is 148.7 times higher than that of TiO_2 (P25) (Fig. 4B).

We tested the catalytic activity of Cu-OL-C for benzene oxidation under the full solar spectrum irradiation with different light intensity (Fig. 4C). At the lower light intensity of 257.8 mW cm^{-2}, Cu-OL-C still shows efficient catalytic activity with the r_{ICO2} of 107.5 μmol g^{-1} min^{-1}. Increasing light intensity significantly enhances the catalytic activity of Cu-OL-C. When the light intensity increases to 268.7, 290.1 mWcm^{-2}, the r_{ICO2} of Cu-OL-C significantly increases to 166.9, 311.6 μmol g^{-1} min^{-1}, respectively.

The catalytic activity of Cu-OL-C for benzene oxidation under the irradiation of visible-infrared or infrared light was measured. Cu-OL-C exhibits efficient catalytic activity under the visible-infrared irradiation. Its r_{ICO2} under the visible-infrared irradiation above 420, 480, 560, and 690 nm is 374.3, 274.0, 200.2, 159.4 μmol g^{-1} min^{-1}, respectively. Even with the infrared irradiation above 830 nm, Cu-OL-C still shows very high catalytic activity with the r_{ICO2} of 123.3 μmol g^{-1} min^{-1} (Fig. 4D).

3.3. Mechanism: solar light driven thermocatalysis

As the Cu doped samples have strong absorption in whole solar spectrum region, the highly efficient catalytic activity of the Cu doped OL-1 sample under the solar light irradiation may originate

from the conventional photocatalysis on photocatalytic semiconductors (e.g. TiO_2) [1,38]. If so, the Cu doped OL-1 samples should have photocatalytic activity at ambient temperature. To clarify the issue, we tested the photocatalytic activity of Cu-OL-C for CO oxidation with the full solar spectrum irradiation under the identical condition used in Fig. 3B besides keeping the reaction temperature at near ambient temperature. In this case, CO can be oxidized to CO_2. Its r_{CO2} is 4.63 μmol g^{-1} min^{-1}, which is 2.8 times higher than that of TiO_2(P25) (1.66 μmol g^{-1} min^{-1}). But compared to its highly efficient photothermocatalytic activity under the full solar spectrum irradiation with the same light intensity at higher temperature (*see the following result and discussion*), its photocatalytic activity (r_{CO2}) at near ambient temperature decreases by 31 times.

It has been reported that nanostructured OL-1 have efficient thermocatalytic activity [49,50]. Therefore, the highly efficient photothermocatalytic activity of the Cu doped OL-1 sample under the solar light irradiation in Figs. 3 and 4 mainly arises from solar light-driven thermocatalysis [42,43] as schematically illustrated in Fig. 5A: Upon the absorption of solar energy, the temperature of the Cu doped OL-1 samples increases owing to photothermal conversion. When the temperature increases above the light-off temperature ($T_{light-off}$) of the thermocatalytic reaction on the Cu doped OL-1 sample, the thermocatalytic reaction occurs.

To confirm the solar light-driven thermocatalysis mechanism, we measured the temperatures of the Cu doped OL-1 samples with the solar light irradiation under the reaction condition as shown in Fig. 3B. Upon the solar light irradiation, owing to efficient photothermal conversion, the temperature of the Cu doped OL-1 sample (Cu-OL-C) quickly increases to an equilibrium temperature (T_{eq}), at which an equilibrium between the solar energy absorption by the sample and the energy dissipation from the sample to the surroundings is established (Fig. 5B). The T_{eq} of OL-1, Cu-OL-A, Cu-OL-B, Cu-OL-C, and Cu-OL-D with the full solar spectrum irradiation is 120, 123, 127, 123, 125 °C, respectively (Fig. 5C). The T_{eq} of Cu-OL-C with the visible-infrared or infrared irradiation above 420, 480, 560, 690, and 830 nm is 120, 115, 111, 105, 100 °C, respectively (Fig. S5). The results indicate that the Cu doped OL-1 samples can efficiently transform the solar energy of UV–vis-infrared, visible-infrared, or infrared light to thermal energy, resulting in the temperature increase.

To prove whether the T_{eq} of the Cu doped OL-1 samples under the solar light irradiation reaches their corresponding $T_{light-off}$ for the thermocatalytic oxidation of CO, we measured the thermocatalytic activity of the Cu doped OL-1 samples for CO oxidation at different temperature in the dark. The pure OL-1 sample exhibits the lowest thermocatalytic activity (Fig. 5D). CO starts to be oxidized when the temperature increases above $T_{light-off}$ = ~100 °C (Table 1). Its reaction temperature of T_{50} and T_{90} (corresponding to 50% and 90% CO conversion) is 157, 194 °C, respectively. The Cu doping in OL-1 results in a considerable increase in the thermocatalytic activity, evidenced by a considerable decrease in the $T_{light-off}$. For all the Cu doped OL-1, CO starts to be oxidized at near ambient temperature ($T_{light-off}$ = ~40 °C). When the Cu/Mn atomic ratio in the OL-1 is 0.028 (Cu-OL-A), its T_{50} and T_{90} are reduced to 130, 159 °C, respectively. When the Cu/Mn atomic ratio in the OL-1 increases from 0.028 to 0.052 (Cu-OL-B), its T_{50} and T_{90} are further reduced to 112, 142 °C, respectively. Cu-OL-C with the Cu/Mn atomic ratio of 0.080 exhibits the highest thermocatalytic activity. Its T_{50} and T_{90} are 103 °C, 135 °C, respectively. Compared to the pure OL-1, the T_{50} and T_{90} of Cu-OL-C are considerably reduced by ΔT_{50} = 54 °C and ΔT_{90} = 59 °C. Cu-OL-D with the Cu/Mn atomic ratio of 0.089 has thermocatalytic activity similar to Cu-OL-C. Its T_{50} and T_{90} are 106, 136 °C, respectively. The considerably enhanced thermocatalytic activity of the Cu doped OL-1 samples is attributed to the fact that increasing the Cu doping amount can promote the activity of lattice oxygen in OL-1, evidenced by CO temperature-programmed reduction (CO-TPR, Fig. S6) and density function theory (DFT) calculation (Fig. S7). The durability of Cu-OL-C for CO oxidation was evaluated. After continuously reacted for 100 h, its thermocatalytic activity remains unchanged (Fig. S8), indicating that the Cu-OL-C sample exhibits excellent catalytic stability.

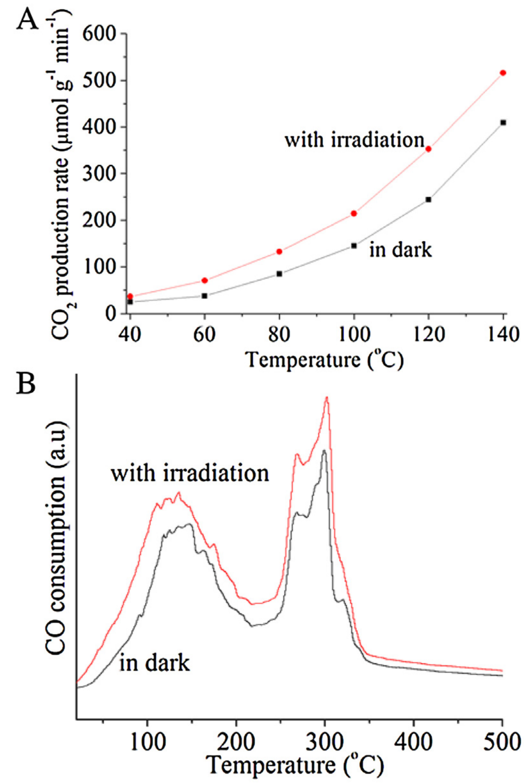

Fig. 6. The catalytic activity of Cu-OL-C for CO oxidation at the different temperature under the condition of 1.0 vol% CO and 96000 mL g$^{-1}{}_{-catal}$ h^{-1} (A). CO-TPR profile of Cu-OL-C in the dark and with the full solar spectrum irradiation (B).

As all $T_{light-off}$ of the Cu doped OL-1 samples (Table 1) is less than their corresponding T_{eq} with the full solar light irradiation (Fig. 5C), and the $T_{light-off}$ of Cu-OL-C is less than its T_{eq} with the visible-infrared or infrared irradiation (Fig. S5), the solar light-driven thermocatalysis on the Cu doped samples can occur. The considerable enhancement in the solar driven thermocatalytic activity of OL-1 upon the Cu doping (Fig. 3B) is attributed to the much higher thermocatalytic activity of the Cu doped OL-1 than OL-1 (Fig. 5D).

3.4. Photoactivation

Does the highly efficient photothermocatalytic activity of the Cu doped OL-1 samples solely arise from the efficient solar light-driven thermocatalysis as discussed above? If yes, the photothermocatalytic activity with the solar light irradiation should be the same as the thermocatalytic activity in the dark at the same reaction temperature. In order to clarify the issue, we tested the catalytic activity of Cu-OL-C for CO oxidation at the same temperature in the dark and with the full solar spectrum irradiation (Fig. 6A). The solar light irradiation considerably enhances the catalytic activity of Cu-OL-C in comparison to its thermocatalytic activity in the dark at the same reaction temperature from 40 to 140 °C. The r_{CO2} of Cu-OL-C with the solar light irradiation at 40, 60, 80, 100, 120, 140 °C is 36.7, 70.6, 132.4, 145.2, 352.6, 515.9 μmol g^{-1} min^{-1}, which is 1.5, 1.9, 1.6, 1.5, 1.3 times higher than their corresponding r_{CO2} in the dark at the same reaction temperature. This result clearly indicates the presence of a photoactivation, thus resulting in the catalytic enhancement upon the solar light irradiation.

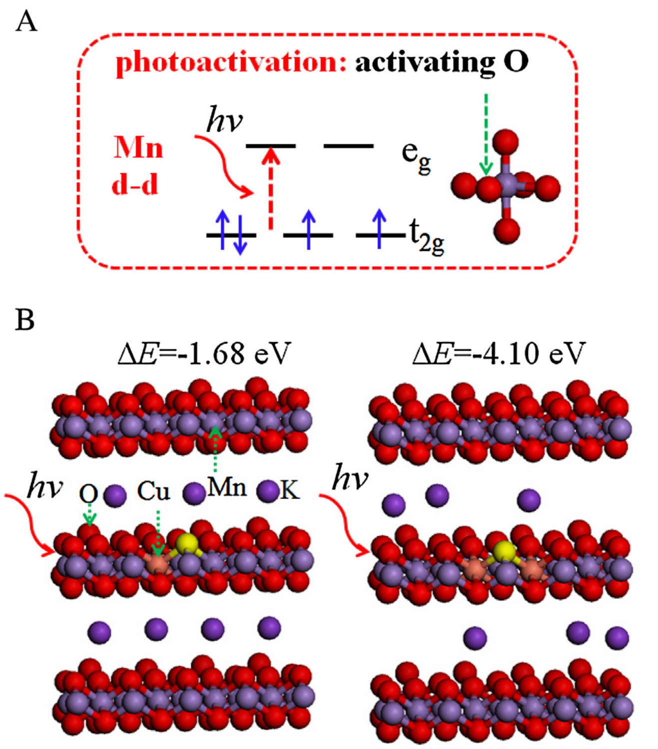

Fig. 7. The schematic illustration of *d-d* transitions (t_{2g}-e_g) of Mn ions in the octahedral site of OL-1 (A). The calculated super cells of Cu doped OL-1 ($K_7Mn_{31}CuO_{64}$ and $K_6Mn_{30}Cu_2O_{64}$) in the excited states (B): yellow sphere represents oxygen atom to be reacted with CO to produce CO_2. (For interpretation of the references to colour in this figure legend, the reader is referred to the web version of this article.)

To reveal the essence of the photoactivation, we investigated the effect of the full solar spectrum irradiation on the CO-TPR behavior of Cu-OL-C. As shown in Fig. 6B, in comparison to the CO-TPR profile of Cu-OL-C in the dark, the solar light irradiation gives rise to an obvious shift of the CO consumption peak below ∼218 °C to lower temperature. This observation suggests that the lattice oxygen of the Cu doped OL-1 becomes active upon the solar light irradiation. Furthermore, the total amount of CO consumption of Cu-OL-C under the solar light irradiation is higher than that in the dark, indicating that more active lattice oxygen is produced upon the solar light irradiation. This result reveals that the photoactivation of the lattice oxygen activity enhanced by the solar light irradiation for the Cu doped OL-1 sample is a novel photoactivation, which is quite different from the conventional photoactivation of the redox reaction trigged by the photogenerated electron in the conduction band and hole in the valence band for the semiconducting photocatalysts (e.g. TiO_2) [1,38].

3.5. DFT calculation

To theoretically confirm the presence of the novel photoactivation effect for the Cu doped OL-1 samples, the effect of the solar light irradiation on the activity of lattice oxygen in the Cu doped OL-1 sample is theoretically studied by DFT calculation. The optical absorption of manganese oxide in the visible region mainly originates from *d-d* transition (t_{2g}-e_g) of Mn ions in the octahedral site [53,54]. Therefore, upon the solar light irradiation, manganese oxide (e.g. OL-1) is promoted to its excited state via the *d-d* transition (Fig. 7A). We calculated the energy of one oxygen atom in the $K_{8-y}Mn_{30-x}Cu_xO_{64}$ super cell in the excited state (upon the solar light irradiation) reacting with a CO molecule:

$$CO + K_{8-y}Mn_{32-x}Cu_xO_{64}*(\text{excited}) = CO_2 + K_{8-y}Mn_{32-x}Cu_xO_{63}*(\text{excited})$$

In order to make such DFT calculation, we employed a constrained occupancy approach of DFT through setting the excitation of one *d* electron to the excited state by increasing the difference between the number of electrons in up and down spin component [55]. The excited states of both CO and CO_2 are not considered in the DFT calculation because they cannot be promoted to their excited states by solar light irradiation.

The ΔE of one oxygen atom in the super cell of $K_7Mn_{31}CuO_{64}$ and $K_6Mn_{30}Cu_2O_{64}$ in the excited state reacting with one CO molecule is −1.68, −4.10 eV (Fig. 7B), which is less than the corresponding value for $K_7Mn_{31}CuO_{64}$ (−1.5 eV) and $K_6Mn_{30}Cu_2O_{64}$ (−3.36 eV) in the ground state (Fig. S7), respectively. This DFT calculation result indicates that the solar light irradiation considerably improves the activity of the lattice oxygen in the Cu doped OL-1. This is in good consistent with the result by CO-TPR in the dark and with the solar light irradiation (Fig. 6B) as discussed above.

4. Conclusion

In summary, the Cu doped OL-1 nanoflowers were prepared by a facile method of hydrothermal redox reaction between $Cu(NO_3)_2$, $Mn(NO_3)_2$, and $KMnO_4$. The Cu doped OL-1 nanoflowers exhibit catalytic activity with very high efficiency with the irradiation of full solar spectrum, visible-infrared, or infrared light. The highly efficient catalytic activity of the Cu doped OL-1 nanoflowers originates from the efficient solar light-driven thermocatalysis, which is attributed to their high thermocatalytic activity as well as their strong absorption in the whole solar spectrum region. The Cu doping in OL-1 significantly increases the thermocatalytic activity of OL-1 owing to the considerable enhancement in the lattice oxygen activity of OL-1 by the Cu doping. A conceptually novel photoactivation is found to enhance the activity of lattice oxygen in OL-1, thus accelerating the solar light-driven thermocatalysis on the Cu doped OL-1. The findings in the present work embark on a novel approach to efficiently use the inexhaustible solar energy for the environmental remediation and the catalytic synthesis of chemicals and fuels, etc.

Acknowledgement

This work was supported by National Natural Science Foundation of China (21473127, 21273169).

Appendix A. Supplementary data

Supplementary data associated with this article can be found, in the online version, at http://dx.doi.org/10.1016/j.apcatb.2016.07.042.

References

[1] A. Kubacka, M. Fernandez-Garcia, G. Colon, Chem. Rev. 112 (2011) 1555–1614.
[2] Y.F. Liu, W.Q. Yao, D. Liu, R.L. Zong, M. Zhang, X.G. Ma, Y.F. Zhu, Appl. Catal. B 163 (2015) 547–553.
[3] N. Zhang, R. Ciriminna, M. Pagliaro, Y.J. Xu, Chem. Soc. Rev. 43 (2014) 5276–5287.
[4] Y.H. Zhang, Z.R. Tang, X.Z. Fu, Y.J. Xu, ACS Nano 4 (2010) 7303–7314.
[5] S.U.M. Khan, M. Al-Shahry, W.B. Ingler Jr., Science 297 (2002) 2243–2245.
[6] R. Asahi, T. Morikawa, T. Ohwaki, K. Aoki, Y. Taga, Science 293 (2001) 269–271.
[7] X.B. Chen, C. Burda, J. Am. Chem. Soc. 103 (2008) 5018–5019.
[8] C.C. Chen, W.H. Ma, J.C. Zhao, Chem. Soc. Rev. 39 (2010) 4206–4219.
[9] N. Shi, X.H. Li, T.X. Fan, H. Zhou, J. Ding, D. Zhang, H.X. Zhu, Energy Environ. Sci. 4 (2011) 172–180.
[10] F. Zuo, L. Wang, T. Wu, Z.Y. Zhang, D. Borchardt, P.Y. Feng, J. Am. Chem. Soc. 132 (2010) 11856–11857.

[11] X.X. Xu, C. Randorn, P. Efstathiou, J.T.S. Irvine, Nat. Mater. 11 (2012) 595–598.
[12] S. Ghosh, N.A. Kouame, L. Ramos, S. Remita, A. Dazzi, A. Deniset-Besseau, P. Beaunier, F. Goubard, P.H. Aubert, H. Remita, Nat. Mater. 14 (2015) 505–511.
[13] X.C. Wang, K. Maeda, A. Thomas, K. Takanabe, G. Xin, J.M. Carlsson, K. Domen, M. Antonietti, Nat. Mater. 8 (2009) 76–80.
[14] P. Christopher, H.L. Xin, S. Linic, Nat. Chem. 3 (2011) 467–472.
[15] L.D. Li, J.Q. Yan, T. Wang, Z.J. Zhao, J. Zhang, J.L. Gong, N.J. Guan, Nat. Commun. 6 (2015) 5881.
[16] M.G. Kibria, F.A. Chowdhury, S. Zhao, B. Alotaibi, M.L. Trudeau, H. Guo, Z. Mi, Nat. Commun. 6 (2015) 6797.
[17] S.S. Chen, Y. Qi, T. Hisatomi, Q. Ding, T. Asai, Z. Li, S.S.K. Ma, F.X. Zhang, K. Domen, C. Li, Angew. Chem. Int. Ed. 54 (2015) 8498–8501.
[18] J. Liu, Y. Liu, N.Y. Liu, Y.Z. Han, X. Zhang, H. Huang, Y. Lifshitz, S.T. Lee, J. Zhong, Z.H. Kang, Science 347 (2015) 970–974.
[19] X.H. Zhang, L.J. Yu, C.S. Zhuang, T.Y. Peng, R.J. Li, X.G. Li, ACS Catal. 4 (2013) 162–170.
[20] J.B. Cui, Y.J. Li, L. Liu, L. Chen, J. Xu, J.W. Ma, G. Fang, E. Zhu, H. Wu, L.X. Zhao, L.Y. Wang, Y. Huang, Nano Lett. 15 (2015) 6295–6301.
[21] Y. Nishijima, K. Ueno, Y. Kotake, K. Murakoshi, H. Inoue, H. Misawa, J. Phys. Chem. Lett. 3 (2012) 1248–1252.
[22] Z.J. Zhang, W.Z. Wang, Dalton Trans. 42 (2013) 12072–12074.
[23] S. Obregon, G. Colon, Chem. Commun. 48 (2012) 7865–7867.
[24] W. Qin, D. Zhang, D. Zhao, L. Wang, K. Zheng, Chem. Commun. 46 (2010) 2304–2306.
[25] X.Y. Wu, S. Yin, Q. Dong, B. Liu, Y.H. Wang, T. Sekino, S.W. Lee, T. Sato, Sci. Rep. 3 (2013) 2918.
[26] C. Li, F. Wang, J. Zhu, J.C. Yu, Appl. Catal. B 100 (2010) 433–439.
[27] Z.X. Li, F.B. Shi, T. Zhang, H.S. Wu, L.D. Sun, C.H. Yan, Chem. Commun. 47 (2011) 8109–8111.
[28] D.X. Xu, Z.W. Lian, M.L. Fua, B.L. Yuanc, J.W. Shi, H.J. Cui, Appl. Catal. B 142 (2013) 377–386.
[29] S.Q. Huang, L. Gu, C. Miao, Z.Y. Lou, N.W. Zhu, H.P. Yuan, A.D. Shan, J. Mater. Chem. A 1 (2013) 7874–7879.
[30] S.Q. Huang, N.W. Zhu, Z.Y. Lou, L. Gu, C. Miao, H.P. Yuan, A.D. Shan, Nanoscale 6 (2014) 1362–1368.
[31] H.T. Li, R.H. Liu, Y. Liu, H. Huang, H. Yu, H. Ming, S.Y. Lian, S.T. Lee, Z.H. Kang, J. Mater. Chem. 22 (2012) 17470–17475.
[32] J. Tiana, Y.H. Leng, Z.H. Zhao, Y. Xi, Y.H. Sang, P. Hao, J. Zhan, M.C. Li, H. Liu, Nano Energy 11 (2015) 419–427.
[33] W. Zou, C. Visser, J.A. Maduro, M.S. Pshenichnikov, J.C. Hummelen, Nat. Photonics 6 (2012) 560–564.
[34] C. Pak, J.Y. Woo, K.H. Lee, W.D. Kim, Y.J. Yoo, D.C. Lee, J. Phys. Chem. C 116 (2012) 25407–25414.
[35] G. Wang, B.B. Huang, X.C. Ma, Z.Y. Wang, X.Y. Qin, X.Y. Zhang, Y. Dai, M.H. Whangbo, Angew. Chem. Int. Ed. 52 (2013) 4810–4813.
[36] Y.H. Sang, Z.H. Zhao, M.W. Zhao, P. Hao, Y.H. Leng, H. Liu, Adv. Mater. 27 (2015) 363–369.
[37] J. Tian, Y.H. Sang, G.W. Yu, H.D. Jiang, X.N. Mu, H. Liu, Adv. Mater. 25 (2013) 5075–5080.
[38] M.R. Hoffmann, S.T. Martin, W.Y. Choi, D.W. Bahnemannt, Chem. Rev. 95 (1995) 69–96.
[39] R.D. Schaller, V.I. Klimov, Phys. Rev. Lett. 92 (2004) 186601.
[40] S.X. Ouyang, J.H. Ye, J. Am. Chem. Soc. 133 (2011) 7757–7763.
[41] F. Liu, M. Zeng, Y.Z. Li, Y. Yang, M.Y. Mao, X.J. Zhao, Adv. Funct. Mater. 26 (2016) 4518–4526.
[42] J.T. Hou, Y.Z. Li, M.Y. Mao, Y.Z. Yue, G.N. Greaves, X.J. Zhao, Nanoscale 7 (2015) 2633–2640.
[43] M.Y. Mao, Y.Z. Li, J.T. Hou, M. Zeng, X.J. Zhao, Appl. Catal. B 174 (2015) 496–503.
[44] J.T. Hou, Y.Z. Li, L.L. Liu, L. Ren, X.J. Zhao, J. Mater. Chem. A 1 (2013) 6736–6741.
[45] J.T. Hou, L.L. Liu, Y.Z. Li, M.Y. Mao, H.Q. Lv, X.J. Zhao, Environ. Sci. Technol. 47 (2013) 13730–13736.
[46] P.E. Blochl, Phys. Rev. B 50 (1994) 17953.
[47] G. Kresse, J. Hafner, Phys. Rev. B 48 (1993) 13115.
[48] C.H. Sun, Y. Wang, J. Zou, S.C. Smith, Phys. Chem. Chem. Phys. 13 (2011) 11325–11328.
[49] S.L. Suib, Acc. Chem. Res. 41 (2008) 479–487.
[50] J.T. Hou, Y.Z. Li, M.Y. Mao, L. Ren, X.J. Zhao, ACS Appl. Mater. Interfaces 6 (2014) 14981–14987.
[51] S. Poulston, P.M. Parlett, P. Stone, M. Bowker, Surf. Interface Anal. 24 (1996) 811–820.
[52] T. Osa, A. Yildiz, T. Kuwana, J. Am. Chem. Soc. 91 (1969) 3994–3995.
[53] N. Sakai, Y. Ebina, K. Takada, T. Sasaki, J. Phys. Chem. B 109 (2005) 9651–9655.
[54] Y.K. Hsu, Y.C. Chen, Y.G. Lin, L.C. Chen, K.H. Chen, J. Mater. Chem. 22 (2012) 2733–2739.
[55] A. Canning, A. Chaudhry, R. Boutchko, N. Gronbech-Jensen, Phys. Rev. B 83 (2011) 125115.